Coherent electron emission from molecules induced by swift ion impact

Nicolas Sisourat, Jérémie Caillat, and Alain Dubois
Laboratoire de Chimie Physique-Matière et Rayonnement, Université Pierre et Marie Curie - CNRS, F-75005 Paris, France

Pablo D. Fainstein
Comisión Nacional de Energía Atómica, Centro Atómico Bariloche, 8400 San Carlos de Bariloche (RN), Argentina
(Received 30 April 2007; published 27 July 2007)

Interference effects for electron emission in collisions between molecules and fast highly charged ions are studied using a nonperturbative semiclassical approach. Angle- and energy-differential results are presented and analyzed as a function of the projectile charge and velocity, as well as the geometric characteristics of the molecular target. They agree qualitatively with the available experimental data and validate the observed primary interference patterns. Contrary to previous theoretical predictions a strong backward-forward asymmetry of the interference structures is found and discussed in detail.

DOI: 10.1103/PhysRevA.76.012718 PACS number(s): 34.10.+x, 34.50.Gb

I. INTRODUCTION

Interference effects are one of the most spectacular signatures of the wavelike nature of particles. From the birth of quantum mechanics they have been analyzed and exploited thoroughly, for example, in atomic and molecular physics: e.g., the so-called "perfect scattering experiments" studies of electron transfer induced by fast ion impact [1,2] or the time-resolved studies of chemical reactions [3]. More recently in attosciences ongoing efforts are performed to monitor the interferences between electronic wave packets created by xuv pulses in order to reconstruct the wave function of atomic or molecular systems [4]. Nanoscale alternatives of the famous Young's double-slit experiment are provided by experiments in which a beam of electrons, ions, or photons ionizes molecules emitting electronic waves which can interfere under appropriate conditions of spatial and temporal coherence. Then the target nuclei play the role of the pinholes and the angle and energy distributions of the ejected electrons may show the expected fringe patterns.

In photoionization processes this effect was first predicted and modeled for molecular hydrogen by Cohen and Fano [5], see also [6] and references therein. To our knowledge, there is no experimental observation of these modulations for H_2 but recent studies have clearly demonstrated their existence for innershell photoionization of heavy homonuclear diatomic molecules such as N_2 [7,8]. In these studies deviations from the expected Young-type modulations were observed and attributed, as in extended x-ray absorption fine structure (EXAFS) spectroscopy, to further interferences stemming from the scattering of the electron ejected from one center by the other. For electron impact induced ionization the interference effects were also predicted and detected experimentally through the analysis of the ejected electron energy and angle distributions [9–11].

For swift highly charged ion impact the Young-type interference effects have been studied thoroughly, starting from their discovery by Stolterfoht and collaborators [12]. These authors measured ionization cross sections as a function of the ejected electron energy for collisions between H_2 and 60 MeV/u Kr^{34+} ions. To get rid of the fast decay of these energy distributions, the authors normalized the experimental cross sections to continuum distorted wave-eikonal initial state (CDW-EIS) results obtained for a hydrogenic target with screened nuclear charge. Clear oscillations (on one period) were observed for ejected electron energies lower than about 300 eV. One dilemma in this first study was connected to the normalization of the experimental data and the possible choices of theoretical data were systematically studied, cf. [13–15]. A very recent study proposed also the normalization of the forward cross sections with the corresponding backward ones [16]. In that context a series of works [14,17,18] was devoted to the study of the angular dependences of the interference patterns, showing (i) weak effects in directions perpendicular to the projectile beam and (ii) evidence for higher frequency of the Young-type oscillations in backward scattering. This was confirmed for H^+ impact at lower energies (1–5 MeV) [19]. However the observed forward-backward asymmetry has not been predicted by theoretical investigations [17], or only as a weaker effect [18,20]. Finally higher frequency oscillations, superimposed on the Young-type structures, have also been observed [19–21]. A tentative explanation involving multiscattering of the electrons before emission, a process giving rise to EXAFS in solid state physics, has been evoked but no theoretical evidence nor definitive interpretation have been given so far.

From the theoretical point of view, the difficulties are related to the correct representation of the bound initial molecular state, the continuum two-center wave function, and the treatment of the dynamics itself, beyond the Born approximation. Besides CDW-EIS treatments within the *effective center* approximation a single nonperturbative approach was proposed in that context [22]. However, this study was based on the classical trajectory Monte Carlo method for which *ad hoc* terms were introduced to take into account the coherence effects not described classically.

In the present paper we propose a detailed investigation of the ionization process for collisions between ions and simple molecular targets (H_2) in a wide range of projectile velocities and charges. In the static and dynamical stages of the calculations we use a nonperturbative semiclassical approach, free of approximations, except for the usual, controllable, numerical accuracy. In order to magnify the weak interference effects and reach converged results, we study low-

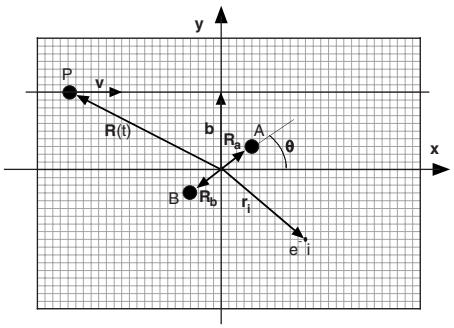

FIG. 1. Collision geometry and schematic (x,y) lattice (grid) representation. $\vec{R}(t)$ defines the projectile trajectory with respect to the target: $\vec{b}$ and $\vec{v}$ are the impact parameter and velocity, respectively. The vector $\vec{r}_i$ locates the electron i on the grid. The angle θ defines the orientation of the molecular internuclear axis $\vec{R}_{ab}=\vec{R}_a-\vec{R}_b$ ($R_{ab}=1.4$ a.u. for the equilibrium internuclear distance) with respect to the projectile velocity $\vec{v}\|0x$. Note that for 1D calculations $b=0$ and $\theta=0$.

dimensional [one dimensional (1D), two dimensional (2D)] ion-molecule collision systems. Such models have been thoroughly used in the past to study laser-atom interaction or ion-atom collisions, e.g., [23–25], and are known to carry all important characteristics of the real systems. The interferences under consideration may as well be analyzed at that level. In Sec. II we present the general formalism adopted to describe the collision system as well as the physical and numerical parameters used in the calculations. Section III is devoted to the presentation of the results, their interpretation, and qualitative comparisons with experimental data. In the following atomic units will be used except when otherwise stated.

II. THEORETICAL MODEL AND IMPLEMENTATION

To model the collisions between H_2 and highly charged ions at impact velocities ranging from 10 a.u. ($\approx$1 MeV/u) to 50 a.u. ($\approx$60 MeV/u) we use the semiclassical approach, within the constant velocity, straight-line trajectory approximation [26], i.e., with the projectile-target relative position vector expressed as $\vec{R}(t)=\vec{b}+\vec{v}t$ (cf. Fig. 1). Moreover, for the impact energies under consideration the interaction time does not exceed one-tenth of a femtosecond so that the nuclei of the molecular target can be considered frozen during the collision (*sudden* approximation). Even though we consider high impact energy collisions, we employ a nonrelativistic treatment since (i) we consider slow emitted electrons and (ii) the Lorentz factor $\gamma_{tp}=1/\sqrt{1-\frac{v^2}{c^2}}$ for the relative target-projectile motion is close to unity ($\gamma_{tp}<1.07$). Under these conditions it has been shown that the relativistic description of the internuclear dynamics does not affect significantly the results, especially when considering electron emission spectra integrated over the projectile momentum transfer (or impact parameter), cf., for example, [27–29]. The time-dependent Schrödinger equation (TDSE)

$$\left[H - i\frac{\partial}{\partial t}\right]\Psi(\vec{r},t) = 0 \tag{1}$$

is then solved fully numerically using spatial Cartesian lattices for one ($1e$) or two ($2e$) active electrons ($\vec{r}\equiv\{\vec{r}_1\}$ or $\vec{r}\equiv\{\vec{r}_1,\vec{r}_2\}$) confined in one (1D) or two (2D) dimensions, i.e., $r_i^2=x_i^2$ or $x_i^2+y_i^2$, respectively. In Eq. (1), the operator H represents the time dependent electronic Hamiltonian which can be written as

$$H = -\frac{1}{2}\nabla_1^2 - \frac{Z_H}{\sqrt{|\vec{r}_1-\vec{R}_a|^2+\alpha^2}} - \frac{Z_H}{\sqrt{|\vec{r}_1-\vec{R}_b|^2+\alpha^2}} - \frac{Z_P}{\sqrt{|\vec{r}_1-\vec{R}(t)|^2+\beta^2}} \tag{2}$$

for one active electron system. Here Z_P is the projectile charge, $\vec{R}_a$ and $\vec{R}_b$ are the position vectors of the two target nuclei (cf. Fig. 1) and Z_H their charge, set to 0.5 to ensure correct asymptotic conditions for the dominant ionization channels. In our implementation we use regularized Coulomb (soft-core) potentials [23] to avoid the singularities at the nuclei and α and β are variational parameters set to match the correct first ionization energies of H_2 and of the projectile, respectively (cf. Table I). For two active electrons the Hamiltonian is

TABLE I. Parameters of the soft-core potentials, of general form $V(r)=-Z/\sqrt{r^2+c^2}$, used to describe the targets and the projectiles, for each of the three models used. E_{ion} is the corresponding first ionization energy expressed in a.u.

	Target			Projectile				
	H_2 ($R_{ab}=1.4$ a.u.)			(Kr^{34+},e^-)			(C^{6+},e^-)	(H^+,e^-)
	1D-1e	2D-1e	1D-2e	1D-1e	2D-1e	1D-2e	1D-1e	1D-1e
Z	0.5	0.5	1.0 and −1.0[a]	34	34	34	6	1
c^2	1.05	0.18	1.18 and 1.0[a]	0.0395	0.0255	0.0395	0.0555	2.0
E_{ion}	0.611	0.611	0.610[b]	144.8	144.6	144.8	18.0	0.50

[a]For the interelectronic repulsive soft-core potential ($\vec{r}\equiv\vec{r}_1-\vec{r}_2$).
[b]$E_{ion}=E_{el}(H_2^+)-E_{el}(H_2)$ at $R_{ab}=1.4$ a.u.

TABLE II. Grid parameters and initial (X_{init}) and final (X_{final}) projectile positions with respect to the target. Note that for the 2D-1e model the characteristics of the grids are the same in the y ($\perp \vec{v}$) direction and that for the 1D-2e model, the grids for both electrons are identical. All values are given in atomic units.

		Grid characteristics				Projectile positions	
Models		x_{min}	x_{max}	n_x	Δx	X_{init}	X_{final}
1D-1e	(a)	−150	+150	2048	0.15	−100	+400
1D-1e	(b)	−500	+500	8192	0.12	−100	+2000
2D-1e		−150	+150	2048	0.15	−100	+400
1D-2e		−150	+150	2048	0.15	−100	+400

$$H = -\frac{1}{2}(\nabla_1^2 + \nabla_2^2) + \frac{1}{\sqrt{|\vec{r}_2 - \vec{r}_1|^2 + \gamma'^2}} - \frac{Z'_H}{\sqrt{|\vec{r}_1 - \vec{R}_a|^2 + \alpha'^2}} - \frac{Z'_H}{\sqrt{|\vec{r}_2 - \vec{R}_a|^2 + \alpha'^2}} - \frac{Z'_H}{\sqrt{|\vec{r}_1 - \vec{R}_b|^2 + \alpha'^2}} - \frac{Z'_H}{\sqrt{|\vec{r}_2 - \vec{R}_b|^2 + \alpha'^2}} - \frac{Z_P}{\sqrt{|\vec{r}_1 - \vec{R}(t)|^2 + \beta^2}} - \frac{Z_P}{\sqrt{|\vec{r}_2 - \vec{R}(t)|^2 + \beta^2}}, \tag{3}$$

where $Z'_H = 1$ and α' and γ' are chosen to get the correct first ionization energies of H_2 and H_2^+ (cf. Table I).

We solve the time-independent Schrödinger equation using the inverse iteration method [30] to obtain the bound states of the isolated target in a spatial lattice of given extension and step sizes Δx and Δy (cf. Table II). Let us remark that this procedure is not used for the projectile Hamiltonian since capture is totally negligible in the energy range considered here. Once the electronic wave function is initialized (at $t=0$) with the ground state of the molecular target the TDSE is numerically integrated by the Crank-Nicolson (CN) scheme [31] on the same lattice: i.e., for a single time step, from t to $t+\Delta t$,

$$|\Psi(t+\Delta t)\rangle \approx e^{-iH(t+\Delta t/2)\Delta t}|\Psi(t)\rangle \tag{4}$$

with Caley's form (Padé approximant [1/1]) for the time-evolution operator

$$e^{-iH(t+\Delta t/2)\Delta t} = \frac{1 - i\frac{1}{2}H\left(t+\frac{\Delta t}{2}\right)\Delta t}{1 + i\frac{1}{2}H\left(t+\frac{\Delta t}{2}\right)\Delta t}. \tag{5}$$

For the 1D-1e model this simply implies to solve tridiagonal systems of linear equations. This is not the case for multidimensional 2D-1e, 1D-2e models for which a splitting of the time-evolution operator is performed,

$$e^{-iH(t+\Delta t/2)\Delta t} \approx e^{-i[T_\alpha + 1/2V(t+\Delta t/2)]\Delta t/2} e^{-i[T_\beta + 1/2V(t+\Delta t/2)]\Delta t} \times e^{-i[T_\alpha + 1/2V(t+\Delta t/2)]\Delta t/2}, \tag{6}$$

where V is the potential energy operator and T_α (T_β) the part of kinetic energy operator corresponding to the x (y) coordinate in the 2D-1e model or to electron 1 (2) in the 1D-2e model. Then Eq. (5) can be applied successively for the three factors of expression (6). This approximation introduces an error in Δt^3 for one step propagation (equivalent to the one generated by the CN algorithm) since the operators defined in Eq. (6) do not commute for 1D-2e and 2D-1e models.

In order to validate our results obtained with the CN scheme we also use the *split-operator* (SO) method [32] to integrate the TDSE, using initial ground states obtained by propagation in imaginary time [33]: we find that the results from both methods are in good agreement. Despite the fact that the SO method can be implemented on vector computers, the results presented in the next section stem only from the CN scheme which provides somewhat more stable results when it comes to weak ionization channels.

Finally it is important to note that we have implemented for each dimension a smooth $\cos(x)^{1/8}$ absorber contributing on a 50 a.u. wide domain around the lattice in order to avoid spurious reflections of the outgoing waves on the border of the grid.

After the propagation stage, the projectile being far away from the target (and outside the lattice, cf. Table II), the total electronic wave function $\Psi(t \to +\infty)$ is analyzed. For active electron calculations, the ionization wave function $|\phi_{ion}\rangle$ is obtained by projecting out the important target bound states ψ_i,

$$|\phi_{ion}\rangle = \left(1 - \sum_i |\psi_i\rangle\langle\psi_i|\right)|\Psi(t \to +\infty)\rangle. \tag{7}$$

For the two-electron calculations, the determination is not straightforward [34] and the single ionization wave function is obtained following a procedure presented in, e.g., [35] where monoelectronic channel functions χ_j are defined as

$$\chi_j(\vec{r}_1) = \int \phi_j^*(\vec{r}_2)\Psi(\vec{r}_1, \vec{r}_2)d\vec{r}_2, \tag{8}$$

where ϕ_j is a given bound state of H_2^+. Single ionization wave functions $\phi_{ion}^{(j)}$ are then obtained by projecting out all bound states of H_2^+ from channel state χ_j,

$$|\phi_{ion}^{(j)}\rangle = \left(1 - \sum_i |\phi_i\rangle\langle\phi_i|\right)|\chi_j\rangle. \tag{9}$$

This wave function describes the single ionization process, assuming the second electron in the state ϕ_j of H_2^+. This procedure can be performed for any states ϕ_j and the total

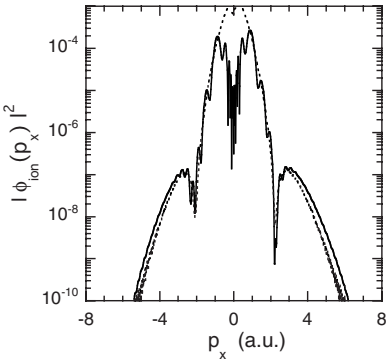

FIG. 2. 1D-1e calculations for Kr^{34+}-H_2 collisions at $v=50$ a.u. ($E\approx 63$ MeV/u). Momentum distribution of the ejected electron: Fourier transform analysis (solid line) and window operator analysis (dotted line). Note that the oscillations seen in results from the first method are commented on in the next section.

ionization wave function ϕ_{ion} is the sum of all possible $\phi_{ion}^{(j)}$. It is worth noting that in the present study the ground state channel function gives the main contribution to single ionization.

Ejected electron momentum distributions are obtained by analyzing the single ionization wave function with either the Fourier transform method [36] or the *window operator* method [37]. In the former it is assumed that the outgoing electrons are far out enough from the target and projectile to be described by plane waves. For the slow electron contribution, this approximation is satisfactory only for very long propagation times and spurious oscillations in the differential results may be observed. The second procedure invoked to analyze the ionization wave function ϕ_{ion} is based on the use of a *window operator* [37] defined as

$$W^{(n)}(E_k,\gamma)=\frac{\gamma^{2^n}}{(H_0-E_k)^{2^n}+\gamma^{2^n}} \tag{10}$$

where H_0 is the target Hamiltonian. The total probability to find ejected electrons with energy in the interval $[E_k-\gamma,E_k+\gamma]$ is given by

$$P^{(n)}(E_k,\gamma)=\langle\phi_{ion}|W^{(n)}|\phi_{ion}\rangle, \tag{11}$$

which can be written as $\gamma^{2^n}\langle\chi_k^{(n)}|\chi_k^{(n)}\rangle$. The probability is then calculated for a wave function by solving a set of linear equations of the form

$$[(H_0-E_k)^{2^{n-1}}-i\gamma^{2^{n-1}}]|\chi_k^{(n)}\rangle=|\phi_{ion}\rangle. \tag{12}$$

For $n=2$ we have

$$(H_0-E_k+\sqrt{i}\gamma)(H_0-E_k-\sqrt{i}\gamma)|\chi_k^{(2)}\rangle=|\phi_{ion}\rangle. \tag{13}$$

For 1D-1e models the Hamiltonian matrix is tridiagonal and Eq. (13) can be straightforwardly solved with a standard linear equation solver package. For 2D-1e and 1D-2e systems the Hamiltonian matrix is banded and very large, and this method is not accurately applicable. Both methods have been checked to agree quite well for 1D-1e systems except at low ejected electron energies ($|p_x|<1$ a.u.), cf. Fig. 2.

III. RESULTS AND DISCUSSION

In order to present clear evidence of the interferences we are going first to show results obtained from the 1D-1e model which allows the magnification of the effects since the electron dynamics is restricted to a single dimension. Note that the momentum distributions presented in this section are the equivalent of the cross sections in the low dimensional spaces considered. These quantities have already been shown to carry the important features of real system dynamics, cf., for example [23,24], and although direct comparisons with measurements are not possible, we have performed calculations for collision systems equivalent to the ones used in the experimental investigations: i.e., the same impact velocities, projectile charges, and target characteristics (ionization energy and internuclear distance). The 1D-1e calculations are numerically fast and stable and involve only one trajectory ($b=0$) and one molecular target orientation ($\theta=0$). In the following the H_2 target is considered at its equilibrium internuclear distance $R_{ab}=1.4$ a.u. Details of the calculations are summarized in Tables I and II, except when otherwise stated.

Figure 3 displays results for Kr^{34+}-H_2 collisions at an impact energy of 63 MeV/u ($v=50$ a.u.), close to the experimental conditions reported in [12,14,20,21]. We show in Fig. 3(a) the total electronic wave function (solid line) after the collision [cf. parameters (a) in Table II], compared with the initial ground state of H_2 (dot-dashed line). As expected it is seen that the ionization process is weak in this regime since (i) in the important central region (around the target nuclei) the wave function remains close to the initial state and (ii) outgoing waves propagate in the forward ($x>0$ and $p_x>0$) and backward ($x<0$ and $p_x<0$) directions with probability density lower than 10^{-5}. A striking feature for the H_2 target is the presence of structures observed in both directions which are not present for the atomic target (dashed line). The positions of density minima, located around $|x|=20$ and 45 a.u., evolve proportionately with time and are the spatial representations of the interference pattern expected from a coherent electron emission from both target nuclei. A signature of these effects can be seen in the momentum distributions shown in Fig. 3(b). For the H_2 target the Fourier analysis of the spatial ionization wave function shows oscillations superimposed on the steep decay of the distributions. They clearly present deep minima located nearly symmetrically in the forward and backward emission directions, at $|p_x|$ equal to about 2, 7, and 11 a.u. In this one-dimensional model the condition for destructive interferences between the electronic waves emitted by both target nuclei can be expressed as

$$(2n+1)\lambda_d=2R_{ab}, \tag{14}$$

where λ_d is the de Broglie wavelength of the electron of momentum $p_x=2\pi/\lambda_d$. For the equilibrium internuclear distance $R_{ab}=1.4$ a.u., this relation predicts values of the electron momentum in very good agreement with the data shown in Fig. 3(b), demonstrating without ambiguity the origin of the oscillations. Contrary to the experimental studies which cannot handle high accuracy on so many orders of magnitude, we have direct evidence of the oscillations on several periods, without the requirement of normalizing the results

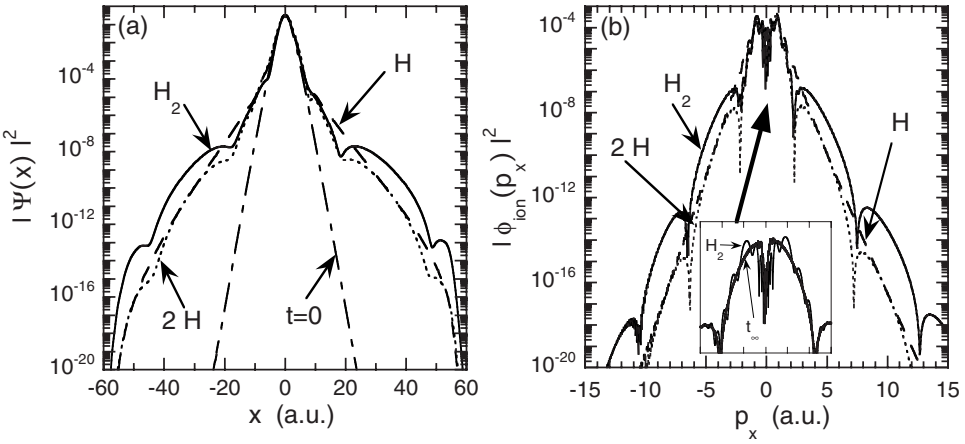

FIG. 3. 1D-1e calculations for Kr^{34+}-H_2 collisions at $v=50$ a.u. ($E\approx 63$ MeV/u). (a) Probability density vs spatial coordinate x. Dot-dashed line: initial ($t=0$) H_2 ground state; solid line: after collision ($t=8$ a.u.); dotted line: after collision, coherent sum for two H atoms at $R=1.4$ a.u; and dashed line: after collision results for the H target. (b) Momentum distribution of the ejected electron. Same as in (a). Inset: magnification of the low energy ($|p_x|<3$ a.u.) part of the distribution. The thick solid line (labeled t_∞) corresponds to $t=200$ a.u.

with monotonically decreasing atomic target data [shown in Fig. 3(b) for H]. Finally note that the present results cannot be directly compared with the experimental data reported in [12,20] but present significant similarities in the location of the first minima ($|p_x|\approx 2.5$ a.u.).

A second demonstration of the origin of this effect can be seen on both frames of Fig. 3: the "2H" curves stem from a model in which we performed the coherent sum of the ionization wave functions from two independent H atoms, located at $R_{ab}=1.4$ a.u. apart from each other. It can be seen that these results, although smaller in magnitude than the H_2 ones because of the different binding energies, present minima exactly located at the same positions. The present "2H" model which uses both an initial ground state and a final continuum state from an atomic (single center) approach, validates the *effective center* approximation used in most of the theoretical treatments so far [12,18].

An additional demonstration of the essential role of the molecular characteristics is given by the analysis of the density minima in terms of the target internuclear distance. We have observed (results not shown) an evolution of the minimum positions in agreement with Eq. (14): for a given order n, the values of p_x for destructive interferences decrease with increasing R_{ab}. Due to the rather narrow range of internuclear distances covered by the H_2 vibrational ground state the interference structures should stay present, though in a less spectacular way, in a treatment taking into account this degree of freedom.

It is worth mentioning the excellent convergence of the results presented in this section, since large box sizes, small mesh steps, and long propagation times were used. However, even in these optimal numerical conditions the momentum distributions oscillate for slow electron emission [see the range $|p_x|<3$ a.u. in the inset of Fig. 3(b)]. These structures are not related to specific physical mechanisms but only due to the fact that the Fourier analysis is performed far from the asymptotic region for the slow electrons; they are indeed not present in the results from the window operator method, cf. Fig. 2. This difficulty which appears in the modeling of ionization processes in grid methods has been previously described in detail by Chassid and Horbatsch [24]. In this work the oscillations were amplified by the fact that the authors were dealing with intermediate projectile velocities ($v=1.5$ a.u.) for which electron capture was not negligible and most of the ejected electrons originated from the *saddle* regime. In our case the use of long propagation times allows for a more satisfactory Fourier analysis. This is illustrated in the inset of Fig. 3(b): the asymptotic [t_∞, cf. line (b) in Table II] results do not present oscillations at small p_x and rapidly converge to the previous results beyond $p_x\approx 2$ a.u. In the following shorter propagation times will be used for calculations requiring important computer resources (2D-1e or 1D-2e models). The data will therefore present at low momentum values fast oscillations whose frequencies cannot be related to the structures observed experimentally.

A further analysis which can be performed with the data of Fig. 3 concerns the asymmetry of the distributions with respect to forward and backward emission. Significant asymmetries have been observed in experimental studies [12,14,16,19,20], where it was found that the frequency of the oscillations is higher in the backward direction (e.g., 150° vs 30° in [19]). No theoretical calculations have been able to explain these results quantitatively. Indeed the model proposed in [17] predicts no asymmetry and the results from [18] show smaller differences between forward and backward cross sections than the one obtained experimentally. However, clear deviations can be observed in our data presented in both frames of Fig. 3 and the destructive interference minima appear for somewhat higher electron velocities in the forward direction, validating the experimental observations. Moreover, the differences between forward and backward scattering are seen to increase with electron velocity: the first minima are located at $p_x\approx -2.1$ and +2.3, the second ones at $p_x\approx -6.5$ and +7.5, the third at $p_x\approx -10.5$ and +12.6, … .

In the following we show that this effect can be explained by phase shifts between the outgoing waves emitted by both target centers. For that purpose we propose a model in which

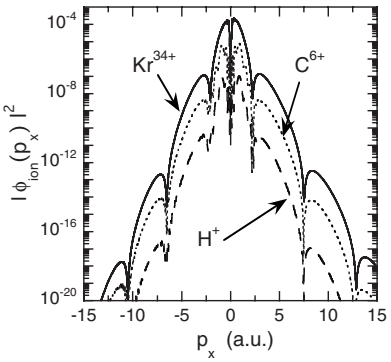

FIG. 4. 1D-1e calculations for X^{q+}-H_2 collisions at $v=50$ a.u. ($\approx$63 MeV/u). Momentum distribution of the ejected electron for three projectiles: Kr^{34+} (solid line), C^{6+} (dotted line), and H^+ (dashed line).

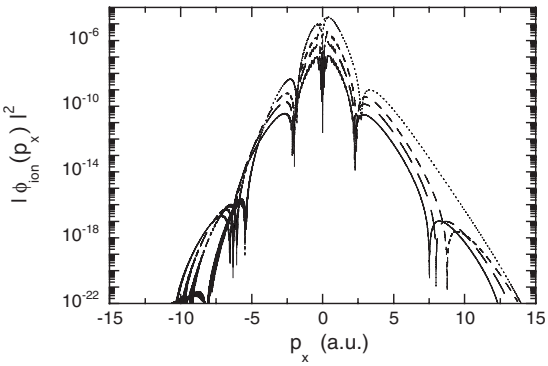

FIG. 5. 1D-1e calculations for H^+-H_2 collisions. Momentum distribution of the ejected electrons for four projectile velocities: $v=50$ a.u. (solid line), $v=30$ a.u. (long dashed line), $v=20$ a.u. (short dash line), and $v=10$ a.u. (dotted line).

the ionization processes from the two centers happen independently, have the same probability, and initiate when the projectile reaches the point of closest approach for each of the nuclei (A and B). The asymptotic outgoing waves can therefore be approximated by plane waves with phase differences related to the position of the two nuclei and the time delay δ to initiate the two ionization channels. For forward (+) and backward (−) scattering the waves can therefore be expressed as

$$\phi_{ion}^{\pm}(x,t) \propto e^{\pm i|p_x|(x-1/2R_{ab})-i1/2p_x^2 t} + e^{\pm i|p_x|(x-1/2R_{ab})-i1/2p_x^2(t-\delta)}, \tag{15}$$

where $\delta=\frac{R_{ab}}{v}$ is the time for the projectile to reach nucleus b after having passed through nucleus a. This gives rise to a probability density which vanishes for values of electron momentum p_x given by the formula

$$|p_x| \pm \frac{p_x^2}{2v} = \frac{(2n+1)\pi}{R_{ab}} \tag{16}$$

which is equivalent to Eq. (14) in the limit of large projectile velocities and small ejected electron momenta. This model quantifies the observed asymmetry for the positions of the minima, which increases with the value of the electron momentum. In fact the values obtained from Eq. (16) agree quantitatively with the results presented in Fig. 3: for $R_{ab}=1.4$ a.u., first minima at $p_x\approx-2.2$ and +2.3, the second one at $p_x\approx-6.3$ and +7.3, the third ones at $p_x\approx-10.2$ and $+12.9,\ldots$. It is worth noting the spectacular quality of the predictions given by this rather simple model.

The dependence with respect to projectile charge and velocity has been partially studied experimentally for impact energies around 1 MeV/u [15,19]. In the following we are going to analyze the dependence of the oscillations with respect to these two parameters: projectile charge for a fixed high velocity and velocity for a fixed low projectile charge. In Fig. 4 ejected electron momentum distributions are displayed for three different projectiles (H^+, C^{6+}, and Kr^{34+}) and the same velocity as in Fig. 3. These data show without ambiguity the invariance of the interference effects and of the forward-backward asymmetry with respect to the projectile charge. The only differences observed are the relative shifts in magnitude between the results, in agreement with the first-Born Z_p^2 scaling. Therefore for this high velocity regime the projectile charge plays no significant role in the formation of the predicted and observed structures.

In Fig. 5 we present results for proton impact and four different impact energies covering the whole range studied experimentally, from 2.5 to 60 MeV/u [38]. A rather smooth evolution of the distributions is observed for decreasing projectile velocity, down to $v=20$ a.u. (10 MeV/u). In this range the minima are clearly identified: the first minima appear almost at the same value of electron momentum for the three velocities, in contrast with the second ones which break up, following the relation given in Eq. (16) and the increase of the dynamical phase shift for decreasing projectile velocities. However, for the smallest selected velocity the shape of the distribution changes drastically with a spectacular forward-backward asymmetry. The absence of second-order minima in the forward direction is related to postcollisional effects (PCEs) which wash out the coherence between the two outgoing waves emitted from both nuclei. However, in the backward direction the electrons move opposite to the projectile and PCEs do not change significantly the shape of the distributions. It is worth noting that the influence of the projectile charge becomes important here, contrary to the conclusion drawn for much higher velocities. The present conclusions corroborate the results discussed in previous studies, e.g., [18,19].

At this point we may conclude that the main effects observed experimentally for different collision systems are confirmed by our results. However, contrary to the experimental investigations in which superimposed oscillations were observed (frequency doubling) [21], our data do not show such structures [39]. Since a multiscattering mechanism, as the one suggested in [21], is explicitly included in our nonperturbative approach, we expected to predict such structures, magnified in our 1D-1e model. This is not the case and it is important before drawing conclusions to go beyond the present 1D calculations and probe further the effects observed experimentally.

Figure 6 shows the differential ionization cross sections calculated from the 2D-1e model for the same collision sys-

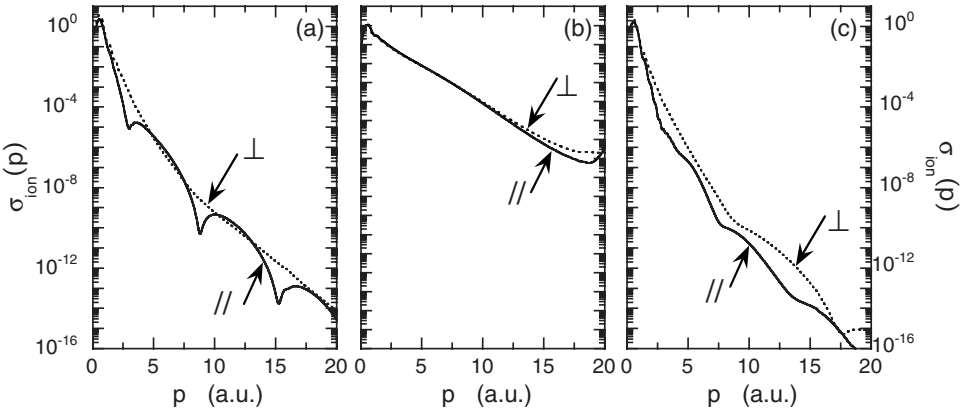

FIG. 6. 2D-1e calculations for Kr^{34+}-H_2 collisions at $v=50$ a.u. ($\approx$63 MeV/u): differential cross sections vs electron momentum for three electron ejection angles and two molecular orientations. Solid line: $\theta=0$ ($\parallel$) and dotted line: $\theta=90°$ ($\perp$). Ejection angles: (a) 30°; (b) 90°; and (c) 150°.

tem as in Fig. 3 (see [40] for the definition of σ_{ion}). The results show the dependence of ionization upon the molecular orientation ($\parallel$ and $\perp$, i.e., H_2 aligned along the x and y axis, respectively) and the electron ejection angle: panel (a) for forward scattering, (b) for 90°, and (c) for backward scattering. Oscillations of the cross sections are again present with well-localized minima, though somewhat less sharp than in the 1D-1e calculations. However, while the interferences manifest clearly for molecules aligned parallel to the impact velocity they are hardly visible for molecules aligned perpendicularly. This can be simply explained by the fact that in this latter configuration the two emitting centers are not equivalent, as assumed in Eq. (15), so that the ionization mainly stems from one of them. As the perpendicular configuration dominates the process, due to a simple geometric argument (e.g., [41]), the interference pattern should be obscured in orientation averaged cross sections, as detected in experimental investigations. For detection at 90°, cf. Fig. 6(b), modulations in cross sections are not present, in agreement with the experimental results [14,19]. In that case the two outgoing waves do not experience phase shifts in the midplane between the two centers so that no interference can indeed be observed. Again no high frequency structures can be seen in our results.

To ensure that no interelectronic effects are responsible for the extra oscillations detected in the experimental cross sections we have performed calculations including two active electrons. To reach a reasonable convergence of the results one has to restrict the description to 1D for each electron so that the overall model is again two-dimensional, as in the paragraph just above. Though the important CPU consumption is equivalent for these two models, the 1D-2e calculations present further complications due to the analysis of the final wave function. This stage has been performed through the procedure described in Sec. II in order to allow the calculation of monoexcited and diexcited molecular states. After projection onto these bound states to extract the ionization wave function, the Fourier transform can be performed to calculate the cross sections. For 63 MeV/u Kr^{34+}-H_2 collisions (see Fig. 7), the main contribution to single ionization is the configuration in which one electron is ionized while the remaining molecular ion, H_2^+, is in its ground state. This allows a simple analysis of the wave function, avoiding the problem of including the autoionizing contribution in the ionization wave function. Figure 7 shows these results together with the ones from the 1D-1e model. The drawbacks of the approximated procedure to get the bound states can be seen in the low electron energy part of the spectrum where the data present spurious oscillations which blur out the expected minima at about $|p_x| \approx 2$ a.u. To avoid these effects we have carried out another analysis of the asymptotic wave function: this procedure is based on the fact that the molecular bound states contribute to Ψ in a well-defined region located around the target. By setting the analyzed wave function Ψ to zero (with no sharp discontinuity) in this zone one can then get rid of the oscillations in the Fourier analysis of the remaining part of the wave function. The momentum distributions obtained from this scheme are also presented in Fig. 7 (labeled with "hole"). The first minima for backward and forward emissions are present there, the significative decrease of the distributions for low electron velocities being explained by the mask operated on the wave function. Considering the interferences effects the agreement between the three sets of data is excellent and no extra structures are again noticeable in this figure.

IV. CONCLUSION

We have performed calculations solving the time-dependent Schrödinger equation in order to obtain accurate, nonperturbative, predictions for ionization channels in fast Z^{q+}-H_2 collisions. Our results confirm the presence of oscillatory structures in the cross sections, in a wide electron energy range (0–3 keV) covering several periods of these

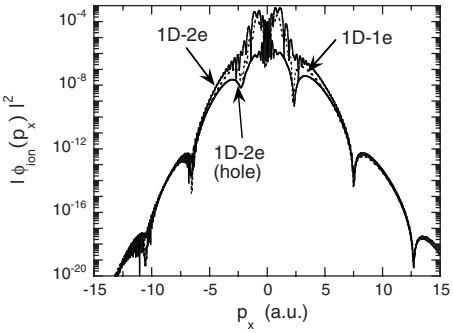

FIG. 7. 1D-2e calculations for Kr^{34+}-H_2 collisions at $v=50$ a.u. ($\approx$63 MeV/u). Momentum distributions: solid line: 1D-2e and dotted line: 1D-1e.

oscillations. Our study provides a complete demonstration of the nature of the involved process: the two centers of the molecular target act as the two holes in the famous Young's experiment and emit waves which interfere for specific geometries and electron momenta. At high impact energies the only parameter which plays a role in the process is the internuclear distance, whereas the projectile charge and velocity only determine the overall magnitude of the ionization probabilities. At lower energies the projectile plays a role, through postcollisional effects, which partly wash out the interference pattern. We have also demonstrated the role of the molecular alignment: it turned out that the modulations observed in measured cross sections are the signature of the ionization process occurring when the molecule is aligned parallel to projectile velocity, i.e., when the two nuclei are equivalent with respect to the ion trajectories. On the other hand our models which include all interactions between the different particles (bound or free) do not show any high frequency structures in the cross sections, unlike experimentally. This is rather surprising and new interpretations should be found to explain the measured data.

ACKNOWLEDGMENTS

This work has been supported by the Direction de la Recherche of Université Pierre et Marie Curie. The Laboratoire de Chimie Physique-Matière et Rayonnement is Unité Mixte de Recherche du l'UPMC et du CNRS (UMR 7614). P.D.F. acknowledges financial support from CONICET and ANPCyT. The computations have been partly performed at Institut du Développement et des Ressources en Informatique Scientifique (IDRIS).

[1] J. Salgado *et al.*, J. Phys. B **30**, 3059 (1997).
[2] J. W. Thomsen *et al.*, J. Phys. B **32**, 5189 (1999).
[3] H. Ihee *et al.*, Science **291**, 458 (2001).
[4] T. Remetter *et al.*, Nat. Phys. **2**, 323 (2006).
[5] H. D. Cohen and U. Fano, Phys. Rev. **150**, 30 (1966).
[6] J. Fernández, O. Fojon, A. Palacios, and F. Martin, Phys. Rev. Lett. **98**, 043005 (2007).
[7] D. Rolles *et al.*, Nature (London) **437**, 711 (2005).
[8] X.-J. Liu *et al.*, J. Phys. B **39**, 4801 (2006).
[9] C. R. Stia *et al.*, J. Phys. B **36**, L257 (2003).
[10] O. Kamalou, J. Y. Chesnel, D. Martina, F. Fremont, J. Hanssen, C. R. Stia, O. A. Fojon, and R. D. Rivarola, Phys. Rev. A **71**, 010702(R) (2005).
[11] D. S. Milne-Brownlie, M. Foster, J. Gao, B. Lohmann, and D. H. Madison, Phys. Rev. Lett. **96**, 233201 (2006).
[12] N. Stolterfoht *et al.*, Phys. Rev. Lett. **87**, 023201 (2001).
[13] M. E. Galassi, R. D. Rivarola, P. D. Fainstein, and N. Stolterfoht, Phys. Rev. A **66**, 052705 (2002).
[14] N. Stolterfoht *et al.*, Phys. Rev. A **67**, 030702(R) (2003).
[15] D. Misra, U. Kadhane, Y. P. Singh, L. C. Tribedi, P. D. Fainstein, and P. Richard, Phys. Rev. Lett. **92**, 153201 (2004); see also J. A. Tanis, S. Hossain, B. Sulik, and N. Stolterfoht, *ibid.* **95**, 079301 (2005); D. Misra, U. Kadhane, Y. P. Singh, L. C. Tribedi, P. D. Fainstein, and P. Richard, Phys. Rev. Lett., **95**, 079302 (2005).
[16] D. Misra, A. Kelkar, U. Kadhane, A. Kumar, L. C. Tribedi, and P. D. Fainstein, Phys. Rev. A **74**, 060701(R) (2006).
[17] L. Nagy, L. Kocbach, K. Póra, and J. P. Hansen, J. Phys. B **35**, L453 (2002).
[18] M. E. Galassi, R. D. Rivarola, and P. D. Fainstein, Phys. Rev. A **70**, 032721 (2004).
[19] S. Hossain, A. L. Landers, N. Stolterfoht, and J. A. Tanis, Phys. Rev. A **72**, 010701(R) (2005).
[20] J. A. Tanis, J. Y. Chesnel, B. Sulik, B. Skogvall, P. Sobocinski, A. Cassimi, J. P. Grandin, L. Adoui, D. Hennacart, and N. Stolterfoht, Phys. Rev. A **74**, 022707 (2006).
[21] N. Stolterfoht, B. Sulik, B. Skogvall, J. Y. Chesnel, F. Fremont, D. Hennecart, A. Cassimi, L. Adoui, S. Hossain, and J. A. Tanis, Phys. Rev. A **69**, 012701 (2004).
[22] L. Sarkadi, J. Phys. B **36**, 2153 (2003).
[23] Q. Su and J. H. Eberly, Phys. Rev. A **44**, 5997 (1991).
[24] M. Chassid and M. Horbatsch, J. Phys. B **31**, 515 (1998).
[25] L. Ponce, R. Taïeb, V. Véniard, and A. Maquet, J. Phys. B **37**, L297 (2004).
[26] W. Fritsch and C. D. Lin, Phys. Rep. **202**, 1 (1991).
[27] C. Pfeiffer, N. Grün, and W. Scheid, J. Phys. B **32**, 53 (1999).
[28] A. B. Voitkiv, B. Najjari, R. Moshammer, M. Schulz, and J. Ullrich, J. Phys. B **37**, L365 (2004).
[29] A. B. Voitkiv and B. Najjari, J. Phys. B **37**, 4831 (2004).
[30] W. H. Press, B. P. Flannery, S. A. Teukolsky, and W. T. Vetterling, *Numerical Recipies* (Cambridge University Press, Cambridge, England, 1989).
[31] J. Crank and P. Nicolson, Proc. Cambridge Philos. Soc. **43**, 50 (1947).
[32] M. D. Feit, J. A. Fleck, and A. Steiger, J. Comput. Phys. **47**, 412 (1982).
[33] A. Kołakowska, M. S. Pindzola, F. Robicheaux, D. R. Schultz, and J. C. Wells, Phys. Rev. A **58**, 2872 (1998).
[34] A. D. Bandrauk and H. Z. Lu, Phys. Rev. A **72**, 023408 (2005).
[35] J. Caillat, J. Zanghellini, M. Kitzler, O. Koch, W. Kreuzer, and A. Scrinzi, Phys. Rev. A **71**, 012712 (2005).
[36] M. Chassid and M. Horbatsch, Phys. Rev. A **66**, 012714 (2002).
[37] K. J. Schafer and K. C. Kulander, Phys. Rev. A **42**, 5794 (1990).
[38] To get same propagation time (about 40 a.u.) for the four velocities, we used larger grids than the ones shown in Table II for the highest projectile velocities, reaching $x_{max}=-x_{min}=2000$ with $n_x=32\,768$, $\Delta x=0.12$, and $X_{final}=2000$ for $v=50$.
[39] We should stress again that the oscillations observed at low electron energies are only due to the short propagation times used in the computations and vanish for increasing ones. Within our conditions (cf. Table II) these artifact oscillations have anyhow higher frequencies than the ones measured.
[40] For the 2D calculations the ionization differential cross section is defined as

$$\frac{d\sigma_{ion}}{d\Omega_e} = \int_0^{+\infty} db |\phi_{ion}(\vec{p})|^2, \tag{17}$$

where $\phi_{ion}(\vec{p})$ is the Fourier transform of the ionization spatial wave function $\phi_{ion}(\vec{r})$ obtained for trajectories characterized by an impact parameter b. Note that these cross sections are impact parameter averaged momentum distributions and cannot be quantitatively compared with experimental data since stemming from a 2D model.

[41] J. Caillat, N. Sisourat, A. Dubois, I. Sundvor, and J. P. Hansen, Phys. Rev. A **73**, 014701 (2006).